

Designing Hybrids of Graphene Oxide and Gold Nanoparticles for Nonlinear Optical Response

Rajesh Kumar Yadav,¹ J. Aneesh,¹ Rituraj Sharma,¹ P. Abhiramath,¹ Tuhin Kumar Maji,² Ganesh Ji Omar,¹
A. K. Mishra,¹ Debjani Karmakar,^{3,*} and K. V. Adarsh^{1,†}

¹*Department of Physics, Indian Institute of Science Education and Research, Bhopal 462066, India*

²*Department of Chemical, Biological and Macromolecular Sciences,*

S. N. Bose National Centre for Basic Sciences, Salt Lake, Kolkata 700 098, India

³*Technical Physics Division, Bhabha Atomic Research Centre, Mumbai 400085, India*



(Received 11 May 2017; revised manuscript received 16 June 2017; published 30 April 2018)

Nonlinear optical absorption of light by materials is weak due to its perturbative nature, although a strong nonlinear response is of crucial importance to applications in optical limiting and switching. Here we demonstrate experimentally and theoretically an extremely efficient scheme of excited-state absorption by charge transfer between donor and acceptor materials as a method to enhance the nonlinear absorption by orders of magnitude. With this idea, we demonstrate a strong excited-state absorption (ESA) in reduced graphene oxide that otherwise shows an increased transparency at high fluence and enhancement of ESA by one order of magnitude in graphene oxide by attaching gold nanoparticles (Au NP) in the tandem configuration that acts as an efficient charge-transfer pair when excited at the plasmonic wavelength. To explain the unprecedented enhancement, we develop a five-level rate-equation model based on the charge transfer between the two materials and numerically simulate the results. To understand the correlation of interfacial charge transfer with the concentration and type of the functional ligands attached to the graphene oxide sheet, we investigate the Au-NP—graphene oxide interface with various possible ligand configurations from first-principles calculations. By using the strong ESA of our hybrid materials, we fabricate liquid cell-based high-performance optical limiters with important device parameters better than that of the benchmark optical limiters.

DOI: [10.1103/PhysRevApplied.9.044043](https://doi.org/10.1103/PhysRevApplied.9.044043)

I. INTRODUCTION

Strong nonlinear optical absorption of photons by materials is a long-standing goal of both fundamental and technological interest, for instance, critical for optical limiting and switching applications [1–4]. The ideal materials for optical-limiting applications must have high transmission at low ambient intensity, reduced transmission at high intensity, and a large dynamic range at which the device damages (irreversibly). Optical-limiting activity has been observed in crystalline and amorphous materials ranging from bulk, thin films, monolayers, and quantum dots [1,3,5–9]. Typical examples are graphene oxide (GO), transition metal dichalcogenides, porphyrin, amorphous chalcogenide thin films, plasmonic materials, etc. [1,3,5–11]. The primary nonlinear absorption processes that are used for optical limiting are multiphoton and excited-state absorptions (ESA) [1–4,12–16]. In multiphoton absorption, the material simultaneously absorbs more than one photon since there is no real resonant single-photon absorption state

[15,16]. This makes the process sensitive to high intensity. On the other hand, ESA is a two-step two-photon absorption process in which the material first absorbs a photon and makes the transition to the allowed resonant single-photon state and in the second step, another photon is absorbed to make the transition to the next allowed single-photon state [13,16]. This step-by-step absorption of two photons through real states occurs in materials only when the excited-state absorption cross section is more than the ground state [16]. Typical examples of materials that show ESA are carbon-based materials such as fullerenes, phthalocyanine complexes, reduced graphene oxide (RGO), graphene oxide (GO), etc. [1,10,13]. Among these, RGO(GO), a thin layer of graphite that contains nonuniform oxygen-containing functional groups is significant because it can surpass the zero-band-gap limitation of graphene [3,12,17,18].

An ESA of RGO(GO) is characterized by the presence of σ states from sp^3 -bonded carbons with oxygen [12,18] that disrupts π states from the sp^2 carbon sites [12,18]. Enhancing the ESA of RGO(GO) nanosheets is of great importance to accomplishing stronger and efficient light-matter interactions for applications such as all-optical deterministic quantum logic and limiting at the nanoscale. Many efforts have been made to improve the ESA of RGO(GO) in the visible-to-IR region, for instance

*To whom all correspondence should be addressed.
debjan@barc.gov.in

†To whom all correspondence should be addressed.
adarsh@iiserb.ac.in

by modifying the electronic and chemical structure through functionalization and doping [1,3,5–8,12–14]. Notwithstanding, the enhancements were minimal. Recent studies have shown that attaching metal (Ag or Au) and semiconducting (ZnO) nanoparticles onto GO can enhance the ESA [19–23]. For example, Kalanoor *et al.* have demonstrated ESA in Ag nanoparticle functionalized graphene composite at a high peak intensity of 13 GW/cm². Notably, below 13 GW/cm², these composites show only saturable absorption [23]. However, studies on Ag-nanoparticle—GO nanocomposite revealed the enhancement by as much as 2.8 times at a peak intensity of 0.2 GW/cm² [21]. Despite observing small enhancements of ESA in Au- or Ag-GO nanocomposites, however, the exact mechanism remains poorly defined. Further, the roles of ligand concentration in controlling the ESA of GO hybrids remain largely unexplored and need to be resolved. Here, we demonstrate experimentally and theoretically an extremely efficient scheme of ESA by charge transfer between Au NP and RGO(GO) as a method to obtain enhancement at low intensities that are not sufficient enough to significantly deplete the ground state of Au NP or RGO(GO). Strikingly, in Au-NP—RGO hybrid structure, we find a strong ESA coefficient $\approx 64 \pm 4$ cm/GW at a moderate peak intensity of 0.16 GW/cm² that is in stark contrast to the saturable absorption of RGO and Au NP when excited at the plasmonic wavelength. However, the enhancements are much lower at other excitation wavelengths. This suggests that the Au-NP—RGO hybrid structure experiences high rates of charge transfer between them when excited at the plasmonic wavelength. Further, we can also observe the enhancement of the ESA coefficient by one order of magnitude at 1.6 GW/cm² in Au-NP—RGO(GO) for plasmonic excitation. Remarkably, ESA coefficients of the hybrids increase with the increase in oxygen functional groups of GO. The unprecedented enhancements of the ESA are numerically simulated by using the five-level charge-transfer model. The charge transfer between the materials is experimentally verified by using the ultrafast pump-probe spectroscopy. Furthermore, the effects of donor-acceptor interactions are analyzed at the Au-NP—RGO(GO) interfaces by varying the functional ligand concentration with the help of first-principles calculations. Finally, we fabricate the liquid cell-based high-performance optical limiter with important device parameters better than that of the benchmark optical limiters.

II. SAMPLE PREPARATION AND PHYSICAL CHARACTERIZATION

A. Synthesis of gold nanoparticles on RGO(GO) nanosheets

We strategize the wet chemical synthesis based on the dispersible template method for synthesizing Au-NP—RGO(GO) colloidal solutions and the detailed procedure

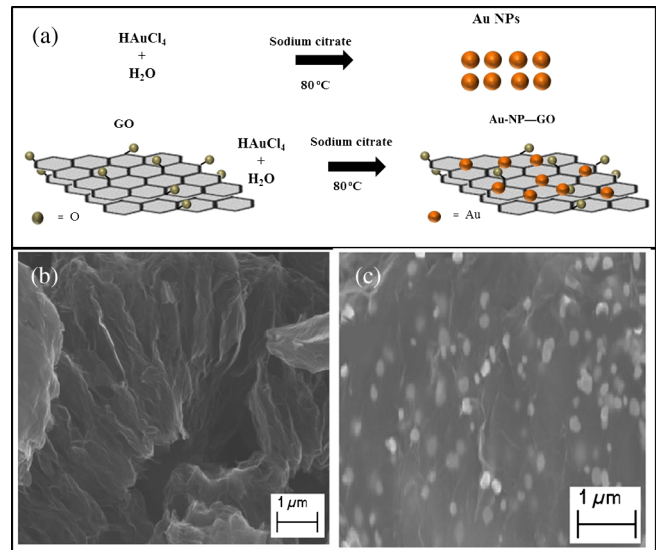


FIG. 1. (a) Schematic representing synthesis of Au NP and Au-NP—GO hybrid, (b) and (c) SEM images of GO and Au-NP—GO hybrid, respectively. The images reveal nanosheet-like morphology of few-layer GO and formation of spherical Au NP over GO nanosheet.

is outlined in Fig. 1(a). In our method, the Au NP is synthesized *in situ* on the RGO(GO) surface by the standard low-cost citrate reduction technique [see Supplemental Material (SM) [24]] [25,26]. This procedure has advantages of high throughput and the flexibility of obtaining nanostructures with controllable size and morphology. The oxygen concentrations name the samples used in the present study as Au-NP—GO, Au-NP—RGO(400), and Au-NP—RGO(1000), and the values inside the bracket show the temperature at which GO is heat treated. The oxygen percentages estimated from the CHN analysis are 61%, 33%, and 12% for Au-NP—GO, Au-NP—RGO(400), and Au-NP—RGO(1000), respectively (Table S1 in SM [24]).

B. Morphological characterization and Raman analysis of Au-NP—RGO(GO)

The powder x-ray diffraction (PXRD) pattern [27–29], scanning electron microscope (SEM) images, and Raman spectra reveal that the samples show excellent crystallinity and the formation of spherical Au NP over RGO(GO) sheets. Figure 1(b) shows SEM images of GO, which confirms nanosheet morphology. Figure 1(c) shows the SEM image of Au-NP—GO, which reveals that the spherical Au NP are anchored over GO. The transmission-electron-microscope image of the Au NP shown in Fig. S1(a) of the SM [24] indicates that the size of the nanoparticles is in the range of 25 ± 3 nm with an overall spherical shape, together with a few larger particles of nonspherical shapes. SEM images of all other samples used in the present study are shown in Fig. S2 of the SM [24]. The LabRAM high-resolution Raman spectrometer with

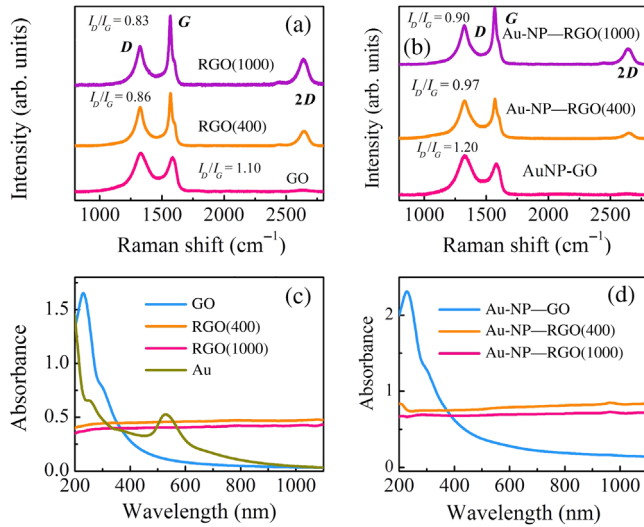


FIG. 2. Raman spectrum of (a) RGO(1000), RGO(400), and GO and (b) Au-NP—RGO(1000), Au-NP—RGO(400), and Au-NP—GO. Optical absorption spectrum of (c) RGO(1000), RGO(400), GO, and Au NP and (d) Au-NP—RGO(1000), Au-NP—RGO(400), and Au-NP—GO. We assume that the strong absorption background of GO and RGO hide the plasmon absorption of Au NP, where the Au NP loading on RGO(GO) is considerably less.

the excitation source at 633 nm from a He-Ne laser in the confocal mode is used to record the Raman spectrum of the samples. Figure 2(a) shows the characteristic *D* mode at 1326 cm⁻¹ and *G* mode at 1580 cm⁻¹ of GO, RGO(400), and RGO(1000). The *D* mode originates from the edges, defects, and disordered carbons, whereas the *G* mode is due to the phonons of the *sp*² C atom of the graphite lattice [30,31]. Apart from the two prominent *D* and *G* modes, we could also observe the weak 2*D* mode at 2645 cm⁻¹. The peak intensity ratio (I_D/I_G) of *D* and *G* modes depends on the degree of disorder and the graphitization of carbonaceous material [30,31]. It can be seen from Fig. 2(a) that I_D/I_G of GO, RGO(400), and RGO(1000) are 1.10, 0.86, and 0.83, respectively. Such an observation clearly indicates the removal of the oxygen-functional groups by our thermal exfoliation process, which is also supported by CHN analysis (SM [24]). It is evident from Fig. 2(b) that the hybrid samples also have the characteristic *D*, *G*, and 2*D* modes at the same frequency of RGO(GO). However, the I_D/I_G ratios show a slight increase as compared to RGO(GO), and the values are displayed in Figs. 2(a) and 2(b). The increases in I_D/I_G values of the hybrids indicate the nucleation of Au NP on the surfaces of RGO(GO) that introduce defects in the structure [30,31].

C. Linear optical response of Au-NP—RGO(GO)

To get a better understanding of the interaction between Au NP and RGO(GO) domains in the hybrid, we first record the optical absorption spectrum of Au NP, GO,

RGO(400), and RGO(1000), as shown in Fig. 2(c). The optical absorption spectrum of Au NP is similar to the previous results that show the plasmon absorption band at 530 nm, which corresponds to the dipolar resonance between the localized plasmon oscillations and the excitation frequency [32]. In contrast, GO exhibit a broad absorption, with two absorption peaks, one at 231 nm due to π -to- π^* transitions in aromatic C = C bonds and the other at 303 nm from *n*-to- π^* transition of carbonyl (C = O) group [8,30]. It can be seen in Fig. 2(c) that RGO(400) and RGO(1000) have broad absorption from 200 to 1100 nm with the optical band gap in the infrared region since oxygen-containing groups forming the *sp*³ matrix are converted into *sp*² clusters, which are in agreement with the published reports [8,30,31]. The optical absorption spectrum of Au-NP—RGO(GO) shown in Fig. 2(d) is exactly similar to the RGO(GO) presented in Fig. 2(c). However, the band corresponding to the plasmonic effect of Au NP is absent. We assume that the strong absorption background of RGO(GO) hides the plasmon band since the Au NP loading on RGO(GO) is less.

III. RESULTS AND DISCUSSION

A. Nonlinear optical response of Au-NP—RGO(GO)

A standard open-aperture Z-scan technique is used to measure the nonlinear optical response of Au-NP—RGO(GO) hybrid structures, which measures the total transmittance as a function of incident laser intensity [16,33,34]. The excitation wavelengths in our experiments are at 1064 and 532 nm, 5-ns pulses from the fundamental and second harmonics of the Nd:YAG laser. The repetition rate of the laser is set at 10 Hz to provide enough time for the system to relax after each pulse. The beam is focused along the Z axis of a computer-controlled translation stage, using a 200-mm focal-length lens. The Rayleigh length (Z_0) and the beam waist of our experiments are 3.2 mm (1064 nm), 1.6 mm (532 nm) and approximately 32 μ m (1064 nm), 17 μ m (532 nm), respectively. For Z-scan measurements, we prepare the dispersions in the distilled water, with a linear transmittance (T) of $\approx 70\%$.

Figure 3(a) shows the Z-scan peak shape of Au-NP—RGO(1000), Au NP, and RGO(1000) at an on-axis peak intensity (measured at the focal point) of 0.16 GW/cm² for 532 nm (plasmon wavelength) excitation. The normalized transmittance of Au-NP—RGO(1000) shows unprecedented nonlinear absorption that is in stark contrast to the saturable absorption of Au NP and RGO(1000). At this moderate intensity, the pristine RGO(1000) and Au NP show saturable absorption since the materials have resonant single-photon absorption states and the peak intensity is not sufficient to make the excited-state absorption cross section more than the ground state. Therefore, we assume that the unprecedented nonlinear absorption of the hybrid is due to the ESA invoked by the charge transfer between the

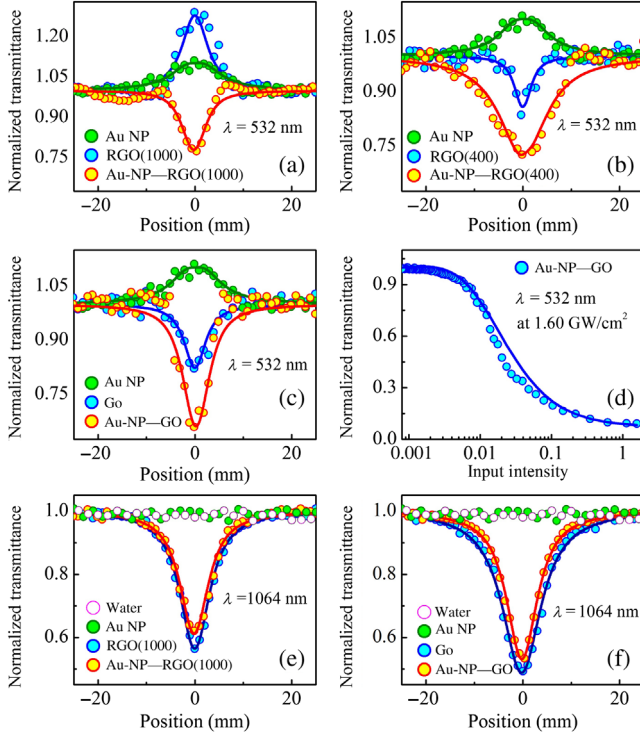


FIG. 3. (a)–(c) Normalized transmittance as a function of position in open-aperture Z scan at 5-ns, 532-nm pulse excitation at a peak intensity of 0.16 GW/cm^2 , for the samples indicated in the panel. (d) Normalized transmittance as a function of input intensity for Au-NP—GO at an input intensity of 1.6 GW/cm^2 . (e),(f) Normalized transmittance as a function of position in open-aperture Z scan at 5-ns, 1064-nm pulse excitation at a peak intensity of 0.35 GW/cm^2 . It is evident from Figs. 3(e) and 3(f) that distilled water has no nonlinear optical response. The solid lines in the figure show the theoretical fitting.

individual components, which was verified later. The Z-scan theory discussed in the SM [24] is used to fit the data to derive the ESA coefficient (β) and saturation intensity (I_s). From the best fit to the normalized transmittance, we find the $\beta_{532 \text{ nm}}$ of Au-NP—RGO(1000) $\approx 64 \pm 4 \text{ cm/GW}$. Next, we select the hybrid samples of Au-NP—RGO(400) and Au-NP—GO, where RGO(400) and GO show ESA. As can be seen in the Fig. 3(b) and Table I, the $\beta_{532 \text{ nm}}$ of Au-NP—RGO(400) $\approx 112 \pm 3 \text{ cm/GW}$, which is found to be ≈ 6 times the RGO(400). Likewise, $\beta_{532 \text{ nm}}$ of Au-NP—GO ($130 \pm 6 \text{ cm/GW}$) is ≈ 6 times GO [Fig. 3(c)]. Figure 3(d) shows the normalized transmittance as the function of input intensity at a peak intensity of 1.6 GW/cm^2 for 532-nm pulse excitation. The nonlinear optical properties of the samples are summarized in Table I. To get more insight on ESA of the Au-NP—RGO(GO) hybrid samples, we perform intensity-dependent Z-scan experiments. As expected from the theory of ESA, $\beta_{532 \text{ nm}}$ of the hybrids show strong intensity dependence (see Table II). Strikingly, we can

TABLE I. Excited-state absorption coefficient (β) and saturation intensity (I_s) calculated by fitting the experimental data with equations shown in SM [24].

Sample	$\beta_{532 \text{ nm}}$ (cm/GW)	$\beta_{1064 \text{ nm}}$ (cm/GW)	$I_{\text{sat}532 \text{ nm}}$ (GW/cm ²)
Au NP	0.05 ± 0.01
RGO(1000)	...	39 ± 5	0.06 ± 0.01
RGO(400)	13 ± 2	46 ± 4	...
GO	18 ± 2	62 ± 6	...
Au-NP—RGO(1000)	64 ± 4	34 ± 4	...
Au-NP—RGO(400)	112 ± 3	40 ± 5	...
Au-NP—GO	130 ± 6	59 ± 6	...

observe enhancements of the ESA by as much as an order of magnitude. For instance, enhancement in Au-NP—RGO(GO) is 6 times at 0.16 GW/cm^2 and 10 times at 1.6 GW/cm^2 . At this stage, we assume that the strong ESA of Au-NP—RGO(GO) is due to the charge transfer between Au NP and RGO(GO) that can be used as a method to enhance the ESA even in materials that show only saturable absorption at moderate intensities.

Before explaining the ESA of the hybrid, we carefully analyze the results of Au NP and RGO(GO). The normalized transmittance of Au NP shows saturable absorption which arises from the depletion of the ground-state surface plasmons since the rate of excitation is much faster than the rate of relaxation to the ground state [35]. Saturable absorption of RGO(1000) is ascribed to the Pauli blocking since the excited state becomes almost occupied, and the Pauli exclusion principle prevents further absorption [8]. Next, we analyze the normalized Z-scan peak shape of RGO(400) and GO, which shows a decrease in transmittance as a function of input intensity. This explains an ESA channel introduced at high intensities that are connected to the sp^3 hybrid states containing oxygen functional groups [8].

TABLE II. Comparison of excited-state absorption coefficient of Au-NP—RGO(GO) hybrid at different peak intensities for 532-nm excitation.

Sample	$\beta_{532 \text{ nm}}$ (cm/GW)		
	0.16 GW/cm ²	0.78 GW/cm ²	1.60 GW/cm ²
Au-NP—RGO(1000)	64 ± 4	115 ± 4	159 ± 6
Au-NP—RGO(400)	112 ± 3	155 ± 5	184 ± 5
Au-NP—GO	130 ± 6	162 ± 5	187 ± 6
RGO(1000)	...	5 ± 2	8 ± 1
RGO(400)	13 ± 2	14 ± 2	16 ± 2
GO	18 ± 2	19 ± 2	20 ± 2

B. Charge transfer between donor-acceptor materials

At this point, it is essential to confirm that the observed enhancement in ESA is due to the synergistic effect of charge transfer between Au NP and RGO(400)/GO. As the first approximation, if RGO(400)/GO and Au NP independently respond to the incoming light, then we should expect a reduction in the ESA. For the range of intensities when $I < I_s$, Eq. (S2) in the SM [24] can be approximated by Taylor expansion to

$$\alpha(I) \approx \alpha_0 + \left(\beta - \frac{\alpha_0}{I_s} \right) I, \quad (1)$$

where $\alpha(I)$ and α_0 are the intensity-dependent absorption coefficient and linear absorption coefficient, respectively. From Eq. (1) it can be seen that $\alpha(I)$ decreases with the increase in intensity. However, in our experiment [Figs. 3(a)–3(c)], we observe an increase in $\alpha(I)$ of the hybrid. Therefore, we come to a logical conclusion that the carriers excited in Au NP through linear absorption, which leads to saturable absorption, should contribute to the ESA in the hybrid.

To confirm the enhancement of ESA is due to charge transfer, we perform the Z-scan experiment at 1064 nm, which is far away from the resonant absorption of Au NP. Excitation of the sample at this wavelength cannot promote the electrons from the Fermi level of Au NP to RGO(GO). In this scenario, it is expected that the ESA of the hybrid is the same as that of RGO(GO) due to the absence of charge transfer. Figures 3(e)–3(f) present the Z-scan traces of the hybrid samples. As expected, we observe that the ESA of Au-NP—RGO(GO) and RGO(GO) are nearly the same within the error bars. These results certainly ascertain our charge-transfer model and demonstrate that strong ESA can be achieved when the hybrid architecture can potentially facilitate light-induced charge transfer. Our results are important in nonlinear optics, where we can customize ESA and design hybrid materials for optical-limiting applications.

C. Ultrafast time-resolved pump-probe spectroscopy of Au-NP—GO hybrid

Most remarkably, our experimental findings suggest that the enhancement of the ESA of the hybrid is primarily due to charge transfer, and therefore to shed more light on this mechanism, we perform broadband transient absorption (TA). In this experiment, the samples are excited with 400-nm, 120-fs pulses of fluence $300 \mu\text{J}/\text{cm}^2$, and the change in absorption of the sample ($\Delta A = -(\log[I_{\text{ex}}/I_0])$) is probed by ultrashort white-light pulses in the wavelength range 450–650 nm. Here, I_{ex} and I_0 are the transmitted intensities of the sequential probe pulses after a delay time τ following excitation by the pump beam, and in the ground state, respectively. Kinetic traces are obtained by varying the path lengths of the probe beam using a micrometer

resolution translation stage and chirp corrected using the procedure reported elsewhere [36]. To avoid the heating effects, the sample is rotated continuously.

TA spectrum of Au-NP—RGO shows a spectrally flat response which is not helpful in analyzing the charge transfer. Figure 4(a) presents the TA spectra of Au-NP—GO, Au NP, and GO at a pump-probe delay of 1 ps. The TA of Au NP and GO are dominated by bleach at the plasmon resonance (530 nm) [37–39] and a broad ESA [8,40], respectively. Detailed analysis of the spectra can be found in the SM [24]. Strikingly, TA of the hybrid sample has a different spectral shape and a distinct time-dependent dynamics [Fig. 4(b)]. First, spectrum of the hybrid is not a simple addition of Au NP and GO at any time within the time scale of our experimental window. Second, the bleach signal below 500 nm shows a redshift with the increase in pump-probe delays. Both features encode information of

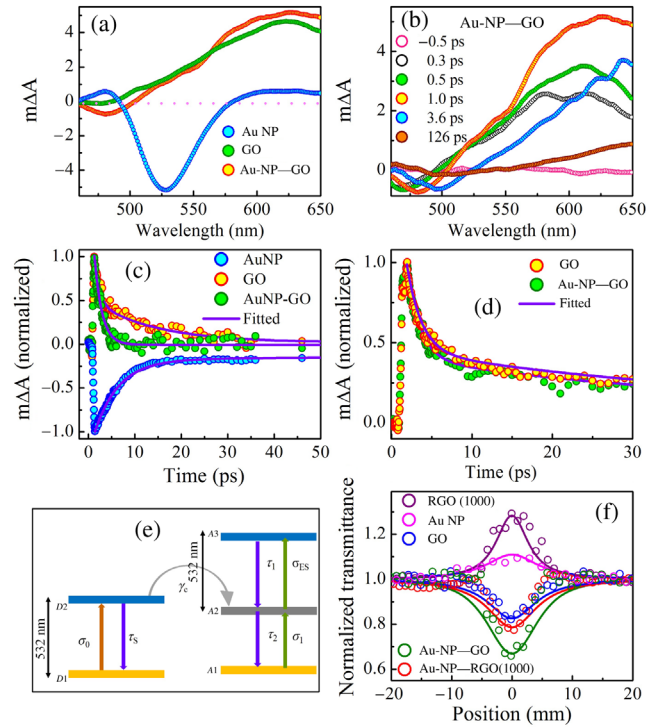


FIG. 4. (a) Spectral evolution of TA spectra of GO, Au NP, and Au-NP—GO hybrid at 1 ps. (b) TA spectra at selected pump-probe delays of Au-NP—GO hybrid, as a function of wavelength. (c) Temporal evolution of TA spectra of GO, Au NP, and Au-NP—GO hybrid integrated over the region 525–540 nm, TA spectra are faster in the case of hybrid compared to GO and Au NP, indicates charge transfer through donor-acceptor interaction. (d) Temporal evolution of TA spectra of GO, Au NP, and Au-NP—GO hybrid at region 600–650 nm. (e) Schematic diagram of charge transfer through donor-acceptor interaction in a five-level model. Here, D_1 and D_2 stand for the ground and excited levels, respectively, of the donor. Similarly, A_1 , A_2 , and A_3 represent the ground, first excited, and second excited levels, respectively, of the acceptor. (f) Shows numerically simulated data which matches with the experimental result.

the net charge transfer between Au NP and GO. In the next step to extract the charge transfer, we plot the integrated area of 525–540 nm of the plasmonic region (to remove the effect of redshift) as a function of time, and the resulting kinetic traces are shown in Figs. 4(c) and 4(d). It can be seen from the figure that the TA of Au-NP—GO is faster than Au NP and GO. To calculate the charge transfer, we assume that the dynamics of TA in the plasmonic region show a difference between the hybrid and Au NP, then the rate of charge transfer (k) can be estimated as $1/\tau_{(\text{Au-NP-GO})} - 1/\tau_{(\text{Au NP})}$ [41,42]. Here, τ is the average lifetime of the decay (see in the SM [24]). By this method, we find the value of $k = (4.3 \pm 0.5) \times 10^{11} \text{ s}^{-1}$.

D. Numerical simulations of five level rate equations through charge transfer

After demonstrating the hallmark observation of the unprecedented enhancement of the ESA due to charge transfer, we develop the five-level rate-equation model shown in Fig. 4(e) to simulate the results numerically. Here, D_1 and D_2 stand for the ground and excited levels, respectively, of the donor. Similarly, A_1 , A_2 , and A_3 represent the ground, first excited, and second excited levels, respectively, of the acceptor. In our model, upon laser illumination, donor Au NP undergoes one-photon absorption and transfers the excited electron to the first excited state A_2 of the acceptor RGO(GO). From the first excited state of the acceptor, it absorbs another photon to go to the second excited state. Such a charge-transfer results in the enhancement of ESA and can be represented by the following coupled rate equations:

$$\frac{dN_{D1}}{dt} = -\frac{\sigma_0 I N_{D1}}{\hbar\omega_0} + \frac{N_{D2}}{\tau_S}, \quad (2)$$

$$\frac{dN_{D2}}{dt} = \frac{\sigma_0 I N_{D1}}{\hbar\omega_0} - \gamma_c N_{D2} - \frac{N_{D2}}{\tau_S}, \quad (3)$$

$$\frac{dN_{A1}}{dt} = -\frac{\sigma_1 I N_{A1}}{\hbar\omega_0} + \frac{N_{A2}}{\tau_2}, \quad (4)$$

$$\frac{dN_{A2}}{dt} = \frac{\sigma_1 I N_{A1}}{\hbar\omega_0} + \gamma_c N_{D2} + \frac{N_{A3}}{\tau_1} - \frac{N_{A2}}{\tau_2} - \frac{\sigma_{ES} I N_{A2}}{\hbar\omega_0}, \quad (5)$$

$$\frac{dN_{A3}}{dt} = \frac{\sigma_{ES} I N_{A2}}{\hbar\omega_0} - \frac{N_{A3}}{\tau_1}. \quad (6)$$

Here, I is incident laser intensity, and subscripts in N (N_{D1} , N_{D2} , N_{A1} , N_{A2} , N_{A3}) represent the respective donor (D) and acceptor (A) levels. The lifetimes $\tau_1 = 0.963$ ps, $\tau_2 = 13.08$ ps, and $\tau_s = 5.17$ ps are obtained from the TA. Absorption cross sections calculated from the Z -scan data [43,44] are listed in Table III. The charge transfer rate (γ_c) is estimated as $(4.3 \pm 0.5) \times 10^{11} \text{ s}^{-1}$ from the TA. The solutions of Eqs. (1)–(6) are obtained numerically by using

TABLE III. Ground-state (σ_0 , σ_1) and excited-state (σ_{ES}) absorption cross sections of Au-NP—RGO(GO) for $\lambda = 532$ nm.

Sample	($\times 10^{-18} \text{ cm}^2$)		σ_{ES} ($\times 10^{-18} \text{ cm}^2$)
	σ_0	σ_1	
Au NP	8.0
RGO(1000)	...	0.13	0.08
RGO(400)	...	0.14	0.16
GO	...	0.15	0.19
Au-NP—RGO(1000)	...	0.59	0.81
Au-NP—RGO(400)	...	0.60	0.96
Au-NP—GO	...	0.61	1.16

a Gaussian pulse in both the temporal and spatial domains. The transmitted intensity through the sample is given by

$$\frac{dI(Z)}{dZ} = [-\sigma_0 N_{D1} - \sigma_1 N_{A1} - \sigma_{ES} N_{A2}] I(Z). \quad (7)$$

Figure 4(f) shows the numerically simulated normalized transmitted intensity through the sample as a function of the position. It can be seen from the figure that our numerical simulations accurately reproduce the experimental results. Therefore, we conclude that the enhancement of the ESA of Au-NP—RGO(GO) is due to the synergistic charge transfer between Au NP and RGO(GO) domains, which can be consistently described by a five-level charge-transfer model. Further, we endeavor to unravel the charge-transfer mechanism at the Au-NP—RGO(GO) interface by scrutinizing their electronic structure.

E. Charge transfer between the Au-NP—RGO(GO) interface from first principles

Although simulating the actual experimental structures of RGO(GO) is extremely complicated, we adopt a simpler scheme to extrapolate the experimental results. To perceive the significance of functional groups in mediating the interlayer coupling of Au-NP—GO, we construct five control systems, viz., (1) graphene nanosheet (G), (2) G with a single hydroxyl (OH) group (G-OH), (3) G with a single carboxylic (COOH) group (G-COOH), (4) G with both OH and COOH groups in lower concentration [GO(low)] and (5) G with both of these groups in higher concentration [GO(high)]. Among these systems, GO(low) and GO(high) are approximate representatives of RGO and GO, respectively. All of these systems are investigated with the help of *ab initio* density-functional-theory- (DFT) based formalism using a plane-wave pseudopotential approach with projector-augmented-wave potentials as implemented in the Vienna *ab initio* simulation package (VASP) [45,46]. Ionic and lattice parameter optimization of the constructed surface and interfaces are obtained by a conjugate gradient algorithm until the Hellmann-Feynman forces on each ion is less than $0.01 \text{ eV}/\text{\AA}$. For self-consistent calculations and

structure optimization, an energy cutoff of 500 eV is used with a k -point mesh size $5 \times 5 \times 3$ with an energy accuracy of 0.0001 eV. The calculation of the electronic charge densities for optimized structures, obtained from VASP calculations, is carried out using the double-zeta plus polarization basis set, as implemented in the ATK 15.1 package [47,48]. Electron correlation within the system is treated using the Perdew-Burke-Ernzerhoff exchange-correlation functional under spin-polarized generalized-gradient approximation (GGA) for all calculations. To account for the interface-induced dipolar interaction, we have incorporated the van der Waal corrections by using the Grimme DFT-D3 method [49]. The details of the theoretical calculation and the control systems (1)–(3) can be found in the SM [24].

Figures 5(a)–5(c) show the atom-projected density of states and orbital-projected density of states of Au-graphene(G), Au-GO(low) and Au-GO(high) interfaces. The observed general trend after comparing the DOS of the control systems (1) to (5), as presented in SM [24], and the corresponding interface with Au, indicates that the originally semiconducting systems with varying band gap turn into metallic ones after combining with the Au layer. The only exception is the system (5), where in addition to strong spin polarization, there is a very small band gap. From Fig. 5(a), we can see that there is charge transfer from the C $2p$ levels of the graphene sheet to Au $6s$ levels, rendering a shift of the Fermi level of the combined system (E_F) towards the valence band by approximately 0.2 eV, which implies a p -type doping of the G sheet. Similar is the

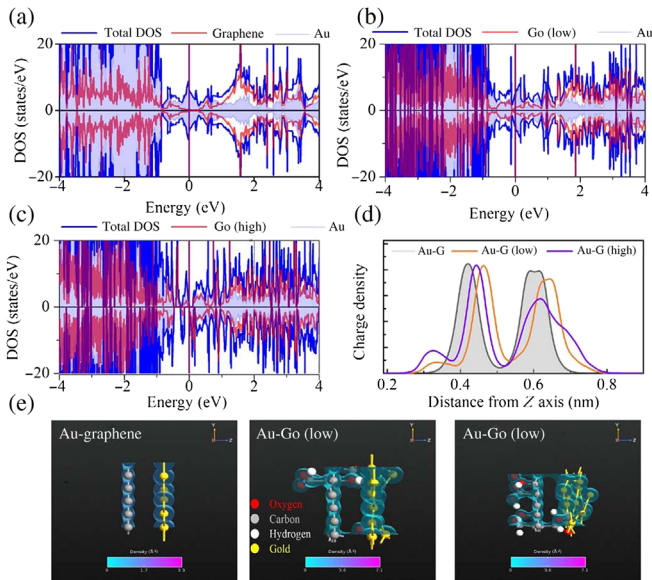


FIG. 5. The atom-projected density of states (APDOS) of (a) Au-G, (b) Au-GO(low), (c) Au-GO(high). All the DOS plots are with respect to $(E - E_F)$. The zero of energy axis is the Fermi level. (d) One-dimensional and (e) three-dimensional charge density projection of Au-G, Au-GO(low), Au-GO(high).

TABLE IV. Shift in Fermi levels (E_F) in comparison to G sheet (ΔE_{F-G}) and GO (ΔE_{F-GO}).

System	ΔE_{F-G}	ΔE_{F-GO}
Graphene (G)
GO(low)	-0.33	...
GO(high)	-0.82	...
Au-G	-0.19	-0.19
Au-GO(low)	-0.29	+0.04
Au-GO(high)	-0.15	+0.67

case with single ligands (G-OH and G-COOH), where the charge transfer occurs from G-OH and G-COOH to Au, with the shift of E_F towards the valence band by approximately 0.2 and 0.1 eV, respectively (SM [24]). However, with an increasing ligand concentration, the E_F shifts towards the conduction band by approximately 0.04 and 0.6 eV, respectively, in Au-GO(low) and Au-GO(high), as in Figs. 5(b) and 5(c). At higher ligand concentration, the structural distortion due to the sp^2 - sp^3 conversion brings the Au layer closer, leading to a charge transfer from Au $6s$ (donor) to C $2p$ (acceptor) via the functional ligands, amounting to n -type doping of the corresponding GO sheet. The respective charge-density profile and the Z -direction projection of the electronic charge density are plotted in Figs. 5(d)–5(e). The first and the second peaks of the Z -direction projection of the electronic charge densities correspond to the GO(G) and the Au layer, respectively. The increase of charge density at the intermediate region and the shift of the peaks indicate the increasing charge transfer with increasing ligand concentration. The quantified shift of E_F all control systems are listed in Table IV. The presence of a higher concentration of ligands for Au-GO(low) and Au-GO(high) introduces an asymmetry in the charge transfer and thus are more spin polarized. Thus, first-principles studies demonstrate the donor-acceptor configurations and indicate the direction of charge transfer in the Au-NP—RGO(GO) systems pointing out its dependence on the concentration and type of functional ligands attached to the GO sheet. For the Au-NP—GO interface with different ligand concentrations, it is indeed possible to modulate the interlayer coupling between the two layers and thereby to control the structural distortion and charge transfer.

F. Liquid-cell-based optical limiter

Clearly, the strong ESA presented here are very large; however, their usefulness would be rather limited without showing a device fabricated based on this idea. To do so, we fabricate a liquid-based optical limiter and the schematic of our device is shown in Fig. 6(a). It essentially consists of a 1-mm path-length liquid cell, that contains the aqueous solution of Au-NP—RGO(GO) as optical-limiting media. We prepare the limiting medium in distilled water,

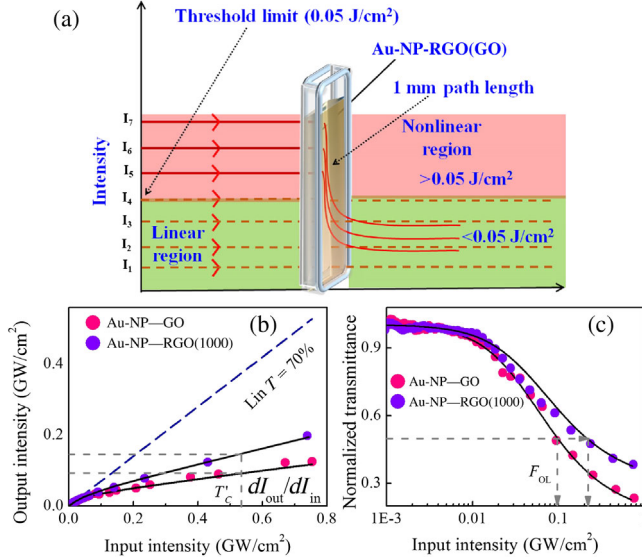


FIG. 6. (a) Schematic of our liquid-based optical-limiting device. It essentially consists of a 1-mm path-length liquid cell, that contains aqueous solution of Au-NP—RGO(GO) acting as optical limiting media. The concentration of the limiting medium in the distilled water is 0.5 mg/ml, with linear transmittance (T) $\approx 70\%$. When the lower intensity beams falls in the linear and safety region (green region), our device will allow the light to pass through. However, above the threshold limit (red region), the system will act as an optical limiter and attenuate the intense beam. (b) Output intensity as a function of input intensity for 532-nm pulse excitation. The dashed and solid lines in the figure show the linear transmittance (T) and the theoretical fitting, respectively. (c) Normalized transmittance as a function of input intensity.

with a linear transmittance (T) of $\approx 70\%$. The device is tested using the Z-scan setup since the optical limiting relies on the fact that the transmission decreases when the input laser intensity is above a threshold. That means the optical-limiting device is designed to keep the linear transmittance below some specified maximum value of input intensity and limit above a certain threshold intensity. To evaluate the device performance, it is essential to characterize the strength of optical limiting using onset threshold F_{on} (the input intensity at which normalized transmittance starts to deviate from linearity), optical-limiting threshold F_{OL} (the input intensity at which normalized transmittance drops below 50%), and limiting differential transmittance T'_C (dI_{out}/dI_{in}) at high intensity.

To demonstrate the optical limiting of our device, we measure the transmitted intensity (I_{out}) as a function of the input intensity (I_{in}) of the laser beam. Figure 6(b) presents a plot of output intensity versus input intensity of our device measured for the 5-ns pulses of wavelength 532 nm up to a peak intensity of 0.78 GW/cm². Our measurements clearly indicate that I_{out} through the device is linearly proportional to I_{in} at a lower intensity. However, with increase in I_{in} , a stage is reached where the I_{out} is no longer linearly

TABLE V. Comparison of nonlinear optical parameters such as F_{on} , F_{OL} , and T'_C of different optical limiters at 532 nm.

System	Lin T	F_{on} (J/cm ²)	F_{OL} (J/cm ²)	T'_C	References
Au-NP—GO	70	0.05	0.49	0.18	Present work
Au-NP—RGO(400)	70	0.05	0.70	0.24	Present work
Au-NP—RGO(1000)	70	0.06	1.09	0.28	Present work
GO	70	0.19	1.19	...	Ref. [50]
MoS ₂ nanosheets	63.8	1.52	11.16	...	Ref. [51]
Graphene nanoribbon	70	0.10	0.70	...	Ref. [52]
CdS nanoparticles	70	0.30	2.55	0.56	Ref. [53]
Pd nanowire	80	0.09	0.90	...	Ref. [54]
Graphene thin film	73	0.01	0.08	0.05	Ref. [1]

proportional to I_{in} , i.e., the deviation of the curve from the linear transmittance. To calculate F_{on} , F_{OL} , and T'_C , we show in Fig. 6(c) the normalized transmittance as a function of the input intensity, and the estimated values are summarized in Table V. Notably, an ideal optical limiter should have very low F_{on} , F_{OL} , and T'_C . From Table V, it can be seen that these important device parameters are better than the benchmark optical limiters such as graphene oxide nanosheets, MoS₂, graphene nanoribbon, CdS nanoparticle, and Pd nanowire [50–54] (Table V), which makes our device an exceptionally good optical limiter. Further, the advantage of our liquid-based optical limiter is that they self-heal, permitting high dynamic ranges limited only by damage to cell windows. In our device, the dynamic range is estimated to be 120 GW/cm².

IV. CONCLUSIONS

Experimental and theoretical results show our scheme of ESA by efficient charge transfer of a donor-acceptor material as a method to enhance the nonlinear absorption in Au-NP—RGO(GO) hybrid materials. At this point, we envision that our current work represents a process in nonlinear optics that explores alternative avenues, ranging from fundamental investigations to technology applications. For example, a fundamental perspective of our study is that the charge transfer occurs from Au NP to GO at higher ligand concentration, and the situation gets reversed at low ligand concentration. The agreement between experimental and theoretical results in our work provides potential test beds for design guidelines to make hybrid structures for enhancing, tuning, and modulating the nonlinear optical response. Additionally, we have fabricated an optical-limiting device based on the liquid cell with important device parameters.

ACKNOWLEDGMENTS

The authors gratefully acknowledge the Department of Science and Technology (Project No. EMR/2016/002520), DAE BRNS (Sanction No. 37(3)/14/26/2016-BRNS/37245). A. K. M. is thankful for support from the INSPIRE faculty Grant No. IFA14-MS-25. T. M. and D. K. acknowledge the BARC ANUPAM supercomputing facility.

- [1] G.-K. Lim, Z.-L. Chen, J. Clark, R. G. S. Goh, W.-H. Ng, H.-W. Tan, R. H. Friend, P. K. H. Ho, and L.-L. Chua, Giant broadband nonlinear optical absorption response in dispersed graphene single sheets, *Nat. Photonics* **5**, 554 (2011).
- [2] M. Z. Alam, I. De Leon, and R. W. Boyd, Large optical nonlinearity of indium tin oxide in its epsilon-near-zero region, *Science* **352**, 795 (2016).
- [3] K. P. Loh, Q. Bao, G. Eda, and M. Chhowalla, Graphene oxide as a chemically tunable platform for optical applications, *Nat. Chem.* **2**, 1015 (2010).
- [4] Q. Bao and K. P. Loh, Graphene photonics, plasmonics, and broadband optoelectronic devices, *ACS Nano* **6**, 3677 (2012).
- [5] Y. Yan, Y. Yuan, B. Wang, V. Gopalan, and N. C. Giebink, Sub-wavelength modulation of $\chi(2)$ optical nonlinearity in organic thin films, *Nat. Commun.* **8**, 14269 (2017).
- [6] A. D. Neira, N. Olivier, M. E. Nasir, W. Dickson, G. A. Wurtz, and A. V. Zayats, Eliminating material constraints for nonlinearity with plasmonic metamaterials, *Nat. Commun.* **6**, 7757 (2015).
- [7] B. J. Eggleton, B. Luther-Davies, and K. Richardson, Chalcogenide photonics, *Nat. Photonics* **5**, 141 (2011).
- [8] R. Sharma, J. Aneesh, R. K. Yadav, S. Sanda, A. R. Barik, A. K. Mishra, T. K. Maji, D. Karmakar, and K. V. Adarsh, Strong interlayer coupling mediated giant two-photon absorption in MoSe₂/graphene oxide heterostructure: Quenching of exciton bands, *Phys. Rev. B* **93**, 155433 (2016).
- [9] Y. Xu, Z. Liu, X. Zhang, Y. Wang, J. Tian, Y. Huang, Y. Ma, X. Zhang, and Y. Chen, Graphene hybrid material covalently functionalized with porphyrin: synthesis and optical limiting property, *Adv. Mater.* **21**, 1275 (2009).
- [10] Z.-B. Liu, Y.-F. Xu, X.-Y. Zhang, X.-L. Zhang, Y.-S. Chen, and J.-G. Tian, Porphyrin and fullerene covalently functionalized graphene hybrid materials with large nonlinear optical properties, *J. Phys. Chem. B* **113**, 9681 (2009).
- [11] S. Zhang, N. Dong, N. McEvoy, M. O'Brien, S. Winters, N. C. Berner, C. Yim, Y. Li, X. Zhang, Z. Chen, L. Zhang, G. S. Duesberg, and J. Wang, Direct observation of degenerate two-photon absorption and its saturation in WS₂ and MoS₂ monolayer and few-layer films, *ACS Nano* **9**, 7142 (2015).
- [12] Z.-B. Liu, X. Zhao, X.-L. Zhang, X.-Q. Yan, Y.-P. Wu, Y.-S. Chen, and J.-G. Tian, Ultrafast dynamics and nonlinear optical responses from Sp²- and Sp³-hybridized domains in graphene oxide, *J. Phys. Chem. Lett.* **2**, 1972 (2011).
- [13] J. W. Perry, K. Mansour, I.-Y. S. Lee, X.-L. Wu, P. V. Bedworth, C.-T. Chen, D. Ng, S. R. Marder, P. Miles, T. Wada, M. Tian, and H. Sasabe, Organic optical limiter with a strong nonlinear absorptive response, *Science* **273**, 1533 (1996).
- [14] M. Kauranen and A. V. Zayats, Nonlinear plasmonics, *Nat. Photonics* **6**, 737 (2012).
- [15] R. W. Boyd, *Nonlinear Optics*, 3rd ed. (Academic Press, Burlington, 2008).
- [16] R. L. Sutherland, *Handbook of Nonlinear Optics*, 2nd ed. (Dekker, New York, 2003).
- [17] T. Musso, P. V. Kumar, A. S. Foster, and J. C. Grossman, Graphene oxide as a promising hole injection layer for MoS₂-based electronic devices, *ACS Nano* **8**, 11432 (2014).
- [18] X.-F. Jiang, L. Polavarapu, S. T. Neo, T. Venkatesan, and Q.-H. Xu, Graphene oxides as tunable broadband nonlinear optical materials for femtosecond laser pulses, *J. Phys. Chem. Lett.* **3**, 785 (2012).
- [19] Thekayat Al Abdulaal and Gregory Salamo, Thermal nonlinearity of functionalized graphene enhanced by gold nanorods, *J. Electr. Eng.* **5**, 171 (2017).
- [20] A. R. Sadrolhosseini, A. S. M. Noor, N. Faraji, A. Kharazmi, and M. A. Mahdi, Optical nonlinear refractive index of laser-ablated gold nanoparticles graphene oxide composite, *J. Nanomater.* **2014**, 1 (2014).
- [21] S. Biswas, A. K. Kole, C. S. Tiwary, and P. Kumbhakar, Enhanced nonlinear optical properties of graphene oxide—Silver nanocomposites measured by Z-scan technique, *RSC Adv.* **6**, 10319 (2016).
- [22] D. Tan, X. Liu, Y. Dai, G. Ma, M. Meunier, and J. Qiu, A universal photochemical approach to ultra-small, well-dispersed nanoparticle/reduced graphene oxide hybrids with enhanced nonlinear optical properties, *Adv. Opt. Mater.* **3**, 836 (2015).
- [23] B. S. Kalanoor, P. B. Bisht, S. Akbar Ali, T. T. Baby, and S. Ramaprabhu, Optical nonlinearity of silver-decorated graphene, *J. Opt. Soc. Am. B* **29**, 669 (2012).
- [24] See Supplemental Material at <http://link.aps.org/supplemental/10.1103/PhysRevApplied.9.044043> for the synthesis method, elemental analysis, morphological characterization, PXRD analysis, Z-scan theory, ultrafast time-resolved pump-probe spectroscopy, the role of functional groups in modulating interlayer coupling of the Au-NP—RGO(GO) interface from first-principles investigation.
- [25] D. C. Marcano, D. V. Kosynkin, J. M. Berlin, A. Sinitskii, Z. Sun, A. Slesarev, L. B. Alemany, W. Lu, and J. M. Tour, Improved synthesis of graphene oxide, *ACS Nano* **4**, 4806 (2010).
- [26] J. Polte, T. T. Ahner, F. Delissen, S. Sokolov, F. Emmerling, A. F. Thünemann, and R. Kraehnert, Mechanism of gold nanoparticle formation in the classical citrate synthesis method derived from coupled *in situ* XANES and SAXS evaluation, *J. Am. Chem. Soc.* **132**, 1296 (2010).
- [27] G. Wang, J. Yang, J. Park, X. Gou, B. Wang, H. Liu, and J. Yao, Facile synthesis and characterization of graphene nanosheets, *J. Phys. Chem. C* **112**, 8192 (2008).
- [28] J. Song, L. Xu, R. Xing, Q. Li, C. Zhou, D. Liu, and H. Song, Synthesis of Au/graphene oxide composites for selective and sensitive electrochemical detection of ascorbic acid, *Sci. Rep.* **4**, 7515 (2014).
- [29] C. Xu, X. Wang, and J. Zhu, Graphene-metal particle nanocomposites, *J. Phys. Chem. C* **112**, 19841 (2008).

- [30] H. Shi, C. Wang, Z. Sun, Y. Zhou, K. Jin, S. A. T. Redfern, and G. Yang, Nonlinear optical absorption of reduced graphene oxide by chemical reduction, *Opt. Express* **22**, 19375 (2014).
- [31] R. Y. N. Gengler, D. S. Badali, D. Zhang, K. Dimos, K. Spyrou, D. Gournis, and R. J. D. Miller, Revealing the ultrafast process behind the photoreduction of graphene oxide, *Nat. Commun.* **4**, 2560 (2013).
- [32] S. Link and M. A. El-Sayed, Size and temperature dependence of the plasmon absorption of colloidal gold nanoparticles, *J. Phys. Chem. B* **103**, 4212 (1999).
- [33] R. K. Yadav, R. Sharma, J. Aneesh, P. Abhiramath, and K. V. Adarsh, Saturable absorption in one-dimensional Sb_2Se_3 nanowires in the visible to near-infrared region, *Opt. Lett.* **41**, 2049 (2016).
- [34] M. Sheik-Bahae, A. A. Said, T.-H. Wei, D. J. Hagan, and E. W. Van Stryland, Sensitive measurement of optical nonlinearities using a single beam, *IEEE J. Quantum Electron.* **26**, 760 (1990).
- [35] H. I. Elim, J. Yang, J.-Y. Lee, J. Mi, and W. Ji, Observation of saturable and reverse-saturable absorption at longitudinal surface plasmon resonance in gold nanorods, *Appl. Phys. Lett.* **88**, 083107 (2006).
- [36] V. I. Klimov and D. W. McBranch, Femtosecond high-sensitivity, chirp-free transient absorption spectroscopy using kilohertz lasers, *Opt. Lett.* **23**, 277 (1998).
- [37] S. Lambright, E. Butaeva, N. Razgoniaeva, T. Hopkins, B. Smith, D. Perera, J. Corbin, E. Khon, R. Thomas, P. Moroz, A. Mereshchenko, A. Tarnovsky, and M. Zamkov, Enhanced lifetime of excitons in nonepitaxial Au/CdS core/shell nanocrystals, *ACS Nano* **8**, 352 (2014).
- [38] T. S. Ahmadi, S. L. Logunov, and M. A. El-Sayed, Picosecond dynamics of colloidal gold nanoparticles, *J. Phys. Chem.* **100**, 8053 (1996).
- [39] S. Link, C. Burda, M. B. Mohamed, B. Nikoobakht, and M. A. El-Sayed, Femtosecond transient-absorption dynamics of colloidal gold nanorods: Shape independence of the electron-phonon relaxation time, *Phys. Rev. B* **61**, 6086 (2000).
- [40] J. Shang, L. Ma, J. Li, W. Ai, T. Yu, and G. G. Gurzadyan, Femtosecond pump-probe spectroscopy of graphene oxide in water, *J. Phys. D* **47**, 094008 (2014).
- [41] J. H. Bang and P. V. Kamat, CdSe quantum dot–fullerene hybrid nanocomposite for solar energy conversion: Electron transfer and photoelectrochemistry, *ACS Nano* **5**, 9421 (2011).
- [42] X. Wen, P. Yu, Y.-R. Toh, Y.-C. Lee, K.-Y. Huang, S. Huang, S. Shrestha, G. Conibeer, and J. Tang, Ultrafast electron transfer in the nanocomposite of the graphene oxide—Au nanocluster with graphene oxide as a donor, *J. Mater. Chem. C* **2**, 3826 (2014).
- [43] Z. Burshtein, P. Blau, Y. Kalisky, Y. Shimony, and M. R. Kikta, Excited-state absorption studies of Cr^{4+} ions in several garnet host crystals, *IEEE J. Quantum Electron.* **34**, 292 (1998).
- [44] Y. Feng, N. Dong, G. Wang, Y. Li, S. Zhang, K. Wang, L. Zhang, W. J. Blau, and J. Wang, Saturable absorption behavior of free-standing graphene polymer composite films over broad wavelength and time ranges, *Opt. Express* **23**, 559 (2015).
- [45] G. Kresse and J. Hafner, *Ab initio* molecular dynamics for liquid metals, *Phys. Rev. B* **47**, 558 (1993).
- [46] G. Kresse and J. Furthmüller, Efficient iterative schemes for *ab initio* total-energy calculations using a plane-wave basis set, *Phys. Rev. B* **54**, 11169 (1996).
- [47] D. R. Smith, S. Schultz, P. Markoš, and C. M. Soukoulis, Determination of effective permittivity and permeability of metamaterials from reflection and transmission coefficients, *Phys. Rev. B* **65**, 195104 (2002).
- [48] J. M. Soler, E. Artacho, J. D. Gale, A. García, J. Junquera, P. Ordejón, and D. Sánchez-Portal, The SIESTA method for *ab initio* order- N materials simulation, *J. Phys. Condens. Matter* **14**, 2745 (2002).
- [49] S. Grimme, Semiempirical GGA-type density functional constructed with a long-range dispersion correction, *J. Comput. Chem.* **27**, 1787 (2006).
- [50] T. He, X. Qi, R. Chen, J. Wei, H. Zhang, and H. Sun, Enhanced optical nonlinearity in noncovalently functionalized amphiphilic graphene composites, *ChemPlusChem* **77**, 688 (2012).
- [51] N. Dong, Y. Li, Y. Feng, S. Zhang, X. Zhang, C. Chang, J. Fan, L. Zhang, and J. Wang, Optical limiting and theoretical modelling of layered transition metal dichalcogenide nanosheets, *Sci. Rep.* **5**, 14646 (2015).
- [52] M. Feng, H. Zhan, and Y. Chen, Nonlinear optical and optical limiting properties of graphene families, *Appl. Phys. Lett.* **96**, 033107 (2010).
- [53] M. Feng, R. Sun, H. Zhan, and Y. Chen, Decoration of carbon nanotubes with CdS nanoparticles by polythiophene interlinking for optical limiting enhancement, *Carbon* **48**, 1177 (2010).
- [54] H. Pan, W. Chen, Y. P. Feng, W. Ji, and J. Lin, Optical limiting properties of metal nanowires, *Appl. Phys. Lett.* **88**, 223106 (2006).